AGU PUBLICATIONS

Geochemistry, Geophysics, Geosystems

RESEARCH ARTICLE
10.1002/2016GC006489

Special Section:
Slow Slip Phenomena and Plate Boundary Processes

Variations in slow slip moment rate associated with rapid tremor reversals in Cascadia

Jessica C. Hawthorne[1], Michael G. Bostock[2], Alexandra A. Royer[2], and Amanda M. Thomas[3]

[1]Institute of Geophysics and Tectonics, School of Earth and Environment, University of Leeds, Leeds, UK, [2]Department of Earth, Ocean and Atmospheric Sciences, University of British Columbia, Vancouver, British Columbia, Canada, [3]Department of Earth Sciences, University of Oregon, Eugene, Oregon, USA

Key Points:
- Observe 50–130% increase in aseismic moment rate during rapid tremor reversals using borehole strain data
- Tremor reversals are associated with *M* 5 aseismic subevents
- Subevents have higher slip rates and smaller stress drops than the main slow slip event

Supporting Information:
- Supporting Information S1

Correspondence to:
J. C. Hawthorne,
J.C.Hawthorne@leeds.ac.uk

Citation:
Hawthorne, J. C., M. G. Bostock, A. A. Royer, and A. M. Thomas (2016), Variations in slow slip moment rate associated with rapid tremor reversals in Cascadia, *Geochem. Geophys. Geosyst.*, *17*, 4899–4919, doi:10.1002/2016GC006489.

Received 21 JUN 2016
Accepted 9 NOV 2016
Accepted article online 14 NOV 2016
Published online 22 DEC 2016

© 2016. American Geophysical Union. All Rights Reserved.

Abstract During large slow slip events, tremor sometimes propagates in the reverse along-strike direction for a few hours, at speeds 10 to 40 times faster than the forward propagation. We examine the aseismic slip that underlies this rapidly propagating tremor. We use PBO (Plate Boundary Observatory) borehole strainmeter data to search for variations in the slow slip moment rate during 35 rapid tremor reversals (RTRs) that occurred beneath Vancouver Island. The strain records reveal that, on average, the strain rate increases by about 100% (±30%) during RTRs. Given the Green's functions expected for slip in the RTR locations, these strain rate increases imply 50 to 130% increases in the aseismic moment rate. The median moment released per RTR is between 8 and 21% of the daily slow slip moment, equivalent to that of a M_W 5.0 to 5.1 earthquake. By combining the RTR moments with the spatial extents suggested by tremor, we estimate that a typical RTR has peak slip of roughly one-sixth of the peak slip in the main slow slip event, near-front slip rate of a few to ten times the main front slip rate, stress drop around half the main event stress drop, and strain energy release rate around one-tenth that of the main front. Our observations support a picture of RTRs as aseismic subevents with high slip rates but modest strain energy release. RTRs appear to contribute to but not dominate the overall slow slip moment, though they may accommodate most of the slip in certain locations.

1. Introduction

A variety of tremor migration patterns has been observed during the large, elongate slow slip events in Cascadia and southwestern Japan. On average, the slow slip events tend to move along strike at rates of 5 to 15 km/d, with up to a factor of a few variability [e.g., *Dragert et al.*, 2001; *Kao et al.*, 2006; *Ide*, 2010; *Ueno et al.*, 2010; *Bartlow et al.*, 2011; *Houston et al.*, 2011]. But within this relatively steady propagation, the tremor migration sometimes reverses for several hours, moving several tens of kilometers back through the region that has already slipped at rates 10–40 times faster than the forward propagation [*Obara*, 2010; *Houston et al.*, 2011; *Royer et al.*, 2015; *Y. Peng et al.*, 2015]. Tremor can also propagate at these speeds over shorter distances, less than 10 or 20 km, in a range of directions [*Rubin and Armbruster*, 2013; *Y. Peng et al.*, 2015]. And in some instances, tremor propagates even faster, moving several tens of kilometers at rates of order 100 km/h, usually along dip [*Ghosh et al.*, 2010a]. Such a range of migration speeds has also been observed in other locations, where slow slip events have less well defined long-term propagation, including along the San Andreas Fault in California [*Ryberg et al.*, 2010; *Shelly*, 2010, 2009; *Z. Peng et al.*, 2015], on the Guerrero subduction zone in Mexico [*Radiguet et al.*, 2012; *Frank et al.*, 2014], and beneath the Central Range in Taiwan [*Sun et al.*, 2015].

Here we investigate several-hour-long intervals of reverse along-strike tremor propagation observed in Cascadia. These rapid tremor reversals (RTRs) typically move 10–50 km over 2–6 h, beginning less than 10 km from the front and moving back through the region that generated tremor in the previous several days [*Obara*, 2010; *Houston et al.*, 2011; *Y. Peng et al.*, 2015; *Royer et al.*, 2015]. There are some indications that RTRs repeat in a preferred location from year to year [*Houston et al.*, 2011; *Royer et al.*, 2015]. A few RTRs even repeat within a single slow slip event. They generate similar tremor patterns about 12 h apart, at times of encouraging tidal stress. Tidal stresses appear to significantly influence the timing of RTRs, causing more reversals to occur when the updip shear stress is larger [*Thomas et al.*, 2013; *Royer et al.*, 2015].

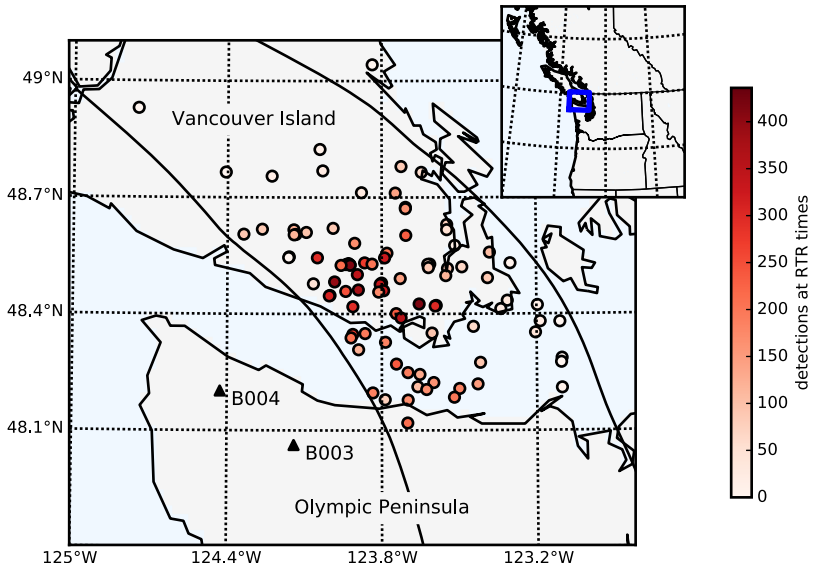

Figure 1. Map of (circles) LFE templates and (triangles) PBO strainmeters. The LFE templates and detections were created by *Bostock et al.* [2012] and *Royer and Bostock* [2014]. Template locations are colored by the number of LFEs detected during RTR time intervals. NW-SE trending curves indicate the 32.5 and 45 km depth contours from *McCrory et al.* [2012]. The inset map illustrates the region of interest, beneath southern Vancouver Island.

Tremor migration patterns like those in RTRs are often interpreted and modeled as indicators of changing aseismic slip rates [*Ando et al.*, 2010; *Luo and Ampuero*, 2011; *Rubin*, 2011; *Ando et al.*, 2012; *Hawthorne and Rubin*, 2013a]. In this context, RTRs may be thought of as subevents that nucleate and spread quickly within the larger slow slip event. Our primary goal here is to estimate the aseismic moment of subevents beneath Vancouver Island.

Constraints on the aseismic moments may help us understand why tremor reversals propagate so quickly: 10–40 times faster than the main front [*Obara*, 2010; *Houston et al.*, 2011; *Royer et al.*, 2015; *Y. Peng et al.*, 2015]. The kinematics of slip coupled with elasticity dictate that the propagation rate V_{prop} of a given front increases with its slip rate V_{slip} and decreases with its stress drop $\Delta\tau$ via [e.g., *Rubin and Ampuero*, 2005; *Shibazaki and Shimamoto*, 2007; *Rubin and Armbruster*, 2013]

$$V_{\text{prop}} = \alpha V_{\text{slip}} \frac{\mu}{\Delta\tau}. \quad (1)$$

Here μ is the shear modulus, and α is a geometric factor of order 1. Thus for RTRs to have faster propagation rates V_{prop} than the main front, RTRs should have higher slip rates, smaller stress drops, or both.

In order to estimate the slip rates and stress drops of RTRs, we couple aseismic moments estimated from PBO borehole strain data with RTR spatial extents estimated from tremor observations. The RTRs were identified by *Royer et al.* [2015] using an extensive catalog of low-frequency earthquakes [*Bostock et al.*, 2012; *Royer and Bostock*, 2014]. We summarize the tremor observations and RTR properties in section 2. In section 3, we introduce the borehole strain data and process it to reduce the nontectonic noise. We identify variations in strain rate associated with RTRs in section 4. Finally, in sections 5 and 6, we estimate the RTR moments and stress drops and discuss the implications for models of slow slip.

2. RTRs in Tremor Observations

The tremor reversals we examine were identified by *Royer et al.* [2015]. They used a low-frequency earthquake (LFE) catalog of tremor detections assembled by *Bostock et al.* [2012] and *Royer and Bostock* [2014] to catalog 64 2–8 h-long intervals of reverse along-strike propagation beneath Vancouver Island. The LFE templates used are shown in Figure 1. We examine 35 RTRs that occurred in 2008, 2010, 2011, and 2012, when RTRs have been identified and high-quality strain data are available.

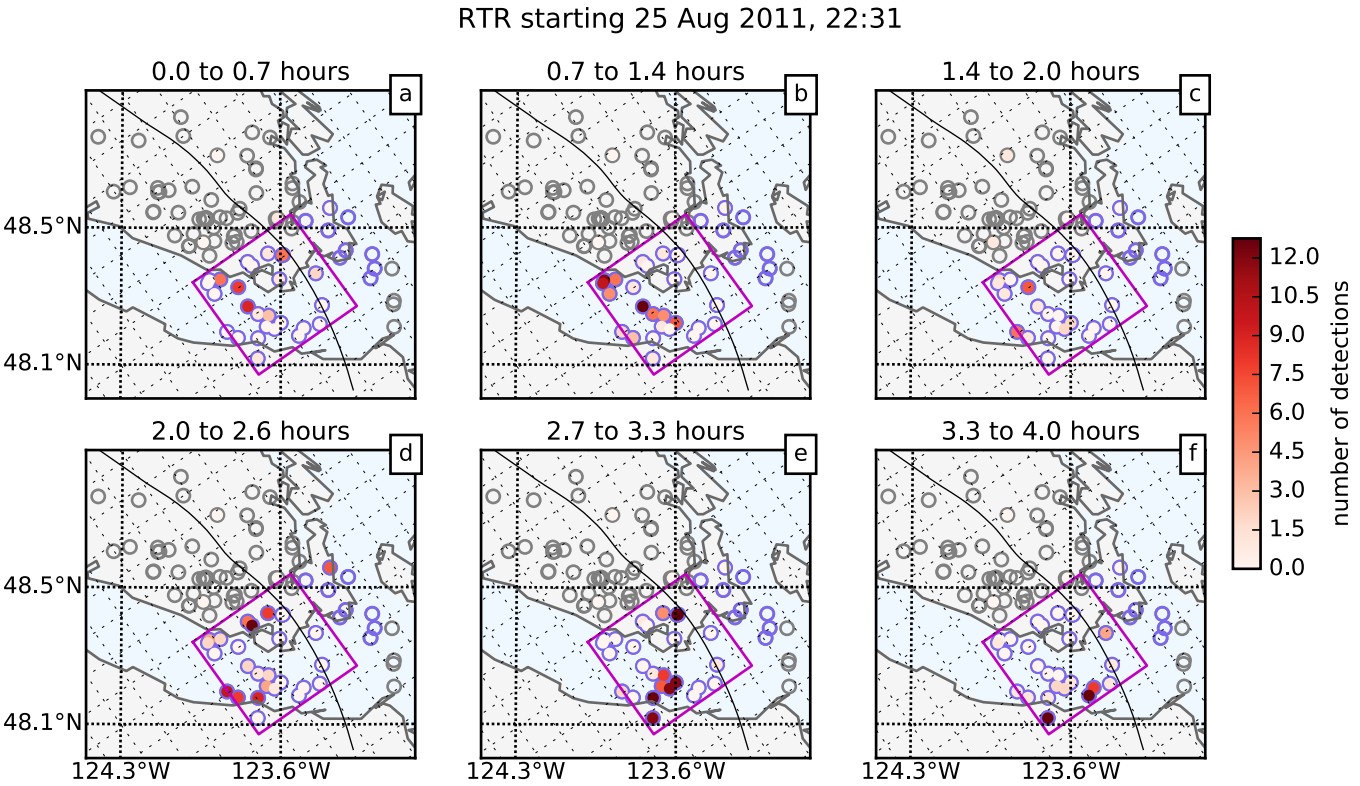

Figure 2. LFE rates and locations during an RTR beginning on 25 August 2011 22:31. In each plot, red shading indicates the number of detections in the specified interval. Blue circles indicate LFEs with detections in the 3 days prior to the RTR, and gray circles indicate the remaining LFE templates [*Bostock et al.*, 2012; *Royer and Bostock*, 2014]. The pink rectangle outlines the RTR region we have identified.

To estimate the RTRs' slips and stress drops, we compare the strain accumulated within RTRs with the spatial extent delineated by tremor. *Royer et al.* [2015] documented the along-strike lengths and along-dip widths of areas which clearly participated in the tremor reversals. Seventy percent of the estimated lengths are between 12 and 22 km, and 70% of the estimated widths are between 7 and 12 km (see supporting information Table S2). However, these lengths and widths are likely to be lower bounds on the RTR dimensions. *Royer et al.* [2015] were conservative in their detections, excluding LFEs that did not clearly match the RTR propagation.

As we seek an estimate of the average slip and stress drop in RTRs, we have no reason to be conservative or liberal in including LFEs in RTRs. We seek unbiased estimates of the RTR spatial extents, not lower or upper bounds. Therefore we re-pick the RTR dimensions. The pink boxes in Figure 2 and supporting information Figures S19–S52 show the identified RTR regions along with the migration of low frequency earthquakes during the reversals. For simplicity, we have assumed that the RTRs are rectangular with one axis along strike, where strike is estimated as the local trend of the 35 km depth contour in the interface model of *McCrory et al.* [2012]. These rectangles seem plausible approximations of most RTR areas, though our imposed geometry may cause us to overestimate some of the spatial extents. Seventy percent of the new lengths and widths are between 10 and 28 km and between 22 and 36 km, respectively, as listed in supporting information Table S2.

The estimated lengths and widths are our best estimates of the dimensions of the several-hour-long RTRs beneath southern Vancouver Island. However, there is subjectivity in estimating the spatial extent of RTRs because tremor propagation is often complex. In Figure 2, for instance, we have excluded the northeastern-most LFE detections from the RTR because they do not follow the main RTR propagation pattern.

A final uncertainty in the RTR locations comes from data coverage. With LFE catalogs, RTRs can be identified only where templates have been created. Cross-station tremor detection methods have found larger along-dip widths for a few reversals [*Savard and Bostock*, 2015]. However, most of the RTRs examined here occur

dominantly in the updip half of the tremor templates, not quite reaching the templates farthest down-dip (*Royer et al*. [2015], and see supporting information Figures S19–S52). Such updip tremor reversals were also observed beneath southern Vancouver Island by *Houston et al*. [2011]. The width of tremor reversals may vary along strike in the Cascadia subduction zone. *Peng and Rubin* [2016] identified RTRs with along-dip widths that vary from about 10–50 km beneath the Olympic Peninsula, south of the region examined here.

3. Strain Data Corrections

To examine the aseismic slip in RTRs, we use strain data recorded by two Plate Boundary Observatory (PBO) borehole strainmeters in Cascadia: B003 and B004 (Figure 1). The borehole strainmeters record horizontal surface strain resulting from slow slip with high precision; instrumental noise is less than one nanostrain. But they also record surface strain due to tides and atmospheric and hydrologic noise with high precision. These unwanted signals must be estimated from the data and removed or avoided. In conventional strainmeter processing, the tidal and atmospheric responses are determined from the strain data and colocated atmospheric pressure records, and then the tidal and atmospheric strains are predicted and removed [e.g., *Tamura et al*., 1991; *Langbein*, 2010].

Here we take a slightly different approach to reducing the nontectonic signals in the strain data. As in conventional processing, we estimate and remove the tidal response. But instead of removing the response to atmospheric pressure, we avoid it. We select and use components of strain that vary minimally as the result of atmospheric pressure changes. We find that using these strain components allows us to reduce not just the noise due to barometric pressure, but also the noise produced by some hydrologic loads.

In this section, we describe the strain data processing and corrections. We will use the corrected data obtained here to look for strain changes associated with RTRs in section 4.

3.1. Premise: Reduced Noise on Nonatmospheric Components

The near-surface strain field recorded by borehole strainmeters can be described using three components of strain. One commonly used set of components is ε_{E+N}, ε_{E-N}, and ε_{2EN}. Here the areal strain ε_{E+N} is the sum of the E-W and N-S extensions, $\varepsilon_E+\varepsilon_N$. The differential extension ε_{E-N} is the difference of these two extensions, $\varepsilon_E-\varepsilon_N$, and the engineering shear $\varepsilon_{2EN}=2\varepsilon_{EN}$ is the east-to-the-north simple shear.

With the PBO borehole strainmeters, these strains are reconstructed as linear combinations of the four horizontal extensometer measurements made in the borehole. Here we reconstruct them using the tidal calibration of *Hodgkinson et al*. [2013]. The data have been quality-controlled and resampled to a 10 min interval by UNAVCO.

The horizontal shear strains ε_{E-N} and ε_{2EN} tend to be less noisy than the areal strain ε_{E+N}. This is likely because the shear strains are less sensitive to spatially extensive and uniform loads. Many potential noise sources, like atmospheric pressure and surface water loading, are roughly uniform on length scales longer than the borehole depth [*Roeloffs*, 2010; *Hodgkinson et al*., 2013]. Because the shear strains are less noisy, previous analysis of slow slip events in Cascadia has focused on the shear strains produced by the slip at depth [e.g., *Wang et al*., 2008; *Hawthorne and Rubin*, 2010; *Dragert and Wang*, 2011; *Hawthorne and Rubin*, 2013b; *Wech and Bartlow*, 2014; *Roeloffs*, 2015].

In this study, we use slightly different strain components. Instead of using the shear strains, which happen to have low noise, we specifically identify components with small atmospheric noise. We choose two strain components with near-zero linear response to barometric pressure variations. These components should also have low response to other noise sources, allowing us to avoid much of the atmospheric and hydrologic noise while still observing the slow slip signals, which can be seen on all components.

The new components we use, which we label as nonatmospheric with "-na," are linear combinations of the original calibrated strains:

$$\varepsilon_{i-na}=B_{i,E+N}\varepsilon_{E+N}+B_{i,E-N}\varepsilon_{E-N}+B_{i,2EN}\varepsilon_{2EN}, \tag{2}$$

where i is $E-N$ or $2EN$, and we have defined a weighting vector $\mathbf{B}_i=[\,B_{i,E+N}\quad B_{i,E-N}\quad B_{i,2EN}\,]^T$. Note that all three of the original strain components ε_{E+N}, ε_{E-N}, and ε_{2EN} respond to atmospheric pressure variations. To

construct new components with small pressure response, we need to choose weights $B_{i,j}$ such that the pressure response cancels as we sum over components.

3.2. Identifying Strain Components With Small Pressure Response

In order to choose the appropriate weights, we must estimate the barometric response on the original components. For each set of strain records (ε_{E+N}, ε_{E-N}, and ε_{2EN}), we first eliminate the largest long-period signals by fitting and removing a constant, linear trend, and decaying exponential from the time series. Then we band-pass filter the data to periods between 4 h and 2 days to isolate signals in the tidal bands. We model the filtered data ε_i according to

$$\varepsilon_i(t) = \underbrace{A_i p(t)}_{\text{pressure}} + \underbrace{\sum_k a_k \cos(\omega_k t) + b_k \sin(\omega_k t)}_{\text{tides}} + \underbrace{(c_{\text{bf}} \cos(t) + d_{\text{bf}} \sin(t)) \frac{t_{\text{af}} - t}{t_{\text{af}} - t_{\text{bf}}} + (c_{\text{af}} \cos(t) + d_{\text{af}} \sin(t)) \frac{t - t_{\text{bf}}}{t_{\text{af}} - t_{\text{bf}}}}_{\text{diurnal signal}}. \quad (3)$$

Here $p(t)$ is atmospheric pressure recorded at a colocated instrument, and A_i is the barometric response on strain component i. The first set of sinusoids represents a tidal correction with between 8 and 21 frequencies ω_k. The number of tidal constituents used is determined according to the noise level, as described in supporting information section S1. We do not exclude the ETS intervals from these fits. While ETS events do produce tidally modulated strain rates, those tidal strains are small, and unlikely to significantly bias our parameter estimations [*Hawthorne and Rubin*, 2010].

The final set of sines and cosines in equation (3) is a diurnal variation resulting from an undetermined source—perhaps surface water loading or a complex pore pressure response to atmospheric pressure. In the data, the diurnal signal varies through time (supporting information Figures S3 and S4), so we parameterize it with a set of nodes spaced every 100 days. We solve for coefficients c and d for each node, and the coefficients used at times between nodes are linearly interpolated from one time to the next. In equation (3), the coefficients c_{bf} and d_{bf} are the coefficients estimated for time t_{bf}, the time of the node just before time t. The coefficients c_{af} and d_{af} are the coefficients estimated for time t_{af}, the time of the node just after time t. Like the strain data, the sinusoids and pressure data are filtered to periods between 4 h and 2 days before the least-squares fit.

The results of equation (3) provide a pressure response for each component, which we place in a pressure response vector for each station: $\mathbf{A} = [A_{E+N} \quad A_{E-N} \quad A_{2EN}]^T$. Any weighting vector $\mathbf{B}_i$ that cancels the atmospheric response must multiply these pressure responses so that they sum to zero; $\mathbf{B}_i \cdot \mathbf{A}$ must equal zero. There are infinite sets of weighting vectors $\mathbf{B}_i$ that can achieve this cancellation. We choose weights to reconstruct two components, ε_{E-N-na} and ε_{2EN-na}, which are as close as possible to the original shear strains ε_{E-N} and ε_{2EN}, respectively. The unnormalized weights $\mathbf{B}_i^u$ are

$$\mathbf{B}^u_{E-N-na} = [0 \quad 1 \quad 0]^T - A_{n,E-N}\mathbf{A}_n \quad (4)$$

$$\mathbf{B}^u_{2EN-na} = [0 \quad 0 \quad 1]^T - A_{n,2EN}\mathbf{A}_n. \quad (5)$$

Here $\mathbf{A}_n$ is the normalized pressure response $\mathbf{A}_n = \mathbf{A}/\sqrt{\mathbf{A}^T\mathbf{A}}$. These weights provide the smallest least-squares difference from the original weights $[0 \quad 1 \quad 0]^T$ and $[0 \quad 0 \quad 1]^T$ while maintaining zero pressure response. Finally, we normalize the weights $\mathbf{B}^u$ to have unit length, obtaining the final weights $\mathbf{B}_i = \mathbf{B}_i^u / \sqrt{(\mathbf{B}^u)_i^T \mathbf{B}_i^u}$ listed in Table 1. For both B003 and B004, the new ε_{E-N-na} is dominated by ε_{E-N}, with weights smaller than 0.1 on the other components. The new ε_{2EN-na} is also dominated by its closest shear strain ε_{2EN}, but it includes slightly larger negative weights, up to −0.5, for ε_{E+N}.

Table 1. The Coefficients $\mathbf{B}_i$ Used to Construct Components That Have Small Atmospheric Response

	E+N	E-N	2EN
B003.E-N-na	0.048	0.999	0.010
B003.2EN-na	−0.205	0.010	0.979
B004.E-N-na	−0.087	0.995	−0.048
B004.2EN-na	−0.481	−0.055	0.875

3.3. Noise in Nonatmospheric Components

The weights successfully eliminate most of the atmospheric pressure response, as well as some nonatmospheric noise. Several examples of the observed signals are shown in the first two rows of Figures 3 and 4. In both figures, plot a shows

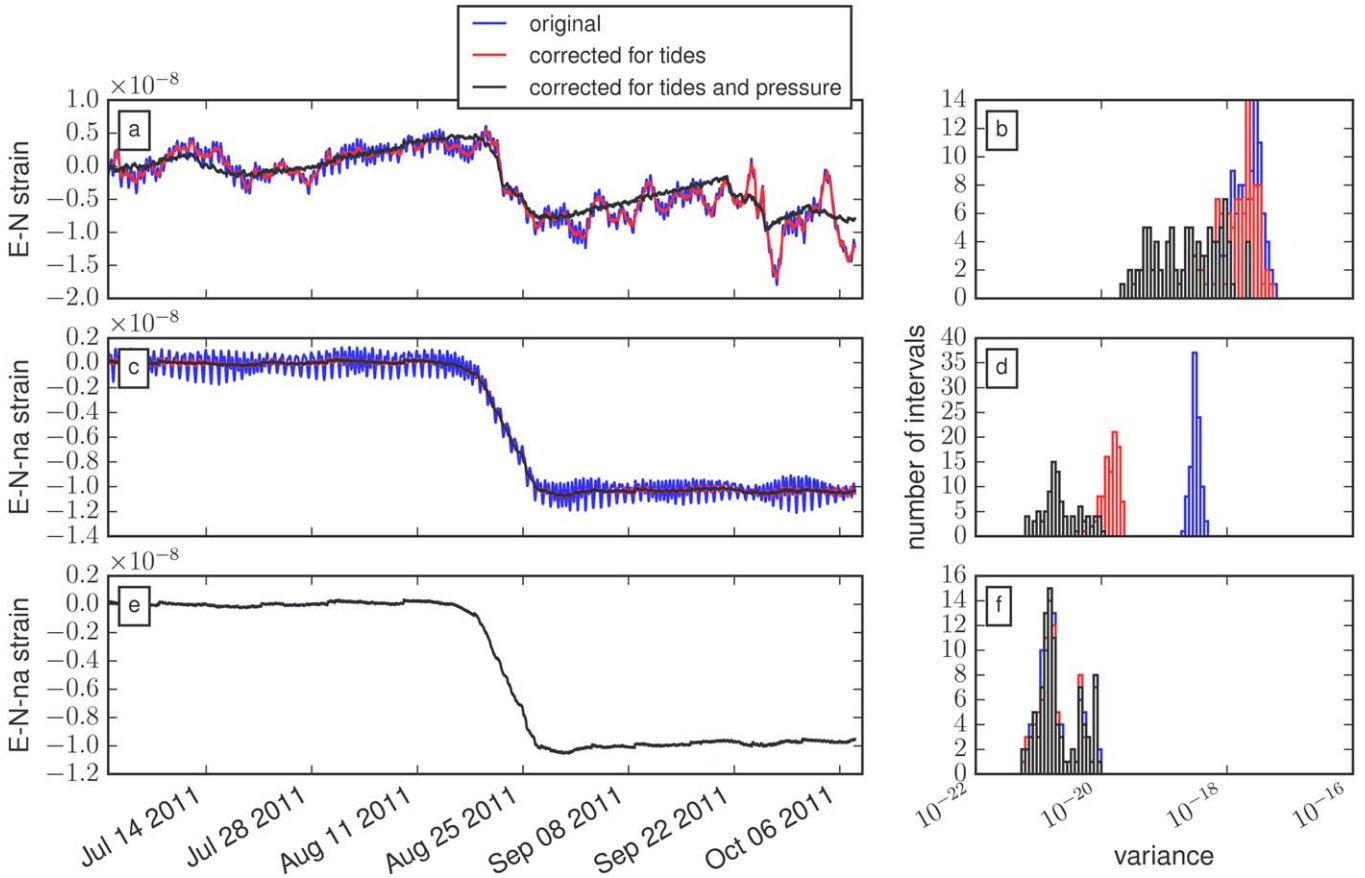

Figure 3. (a) Original ε_{E-N} at strainmeter B004 during the August 2011 slow slip event. The data are uncorrected (blue), corrected for tides (red), and corrected for tides and atmospheric pressure (black). (b) Histograms of variance in 100 day segments in the 6 h to 5 day band. Colors are as in Figure 3a. (c) Original and corrected data, as in Figure 3a, but for a component of strain with minimal atmospheric response, ε_{E-N-na}. (d) Distribution of the variance in 100 day segments for ε_{E-N-na}. (e and f) As in Figures 3c and 3d, but starting with the data corrected for tides and diurnal variations over the entire length of the record.

data from one of the original shear strains. The data are uncorrected (blue), corrected for tides (red), and corrected for tides and atmospheric pressure (black). Plot c shows the same sets of strains, but for a component with minimal atmospheric response. In both plots, corrections are done just for this 100 day interval, and only the five largest tidal constituents are used, with frequencies 0.9295 (for O1), 1.0027 (K1), 1.896 (N2), 1.9323 (M2), and 2 day^{-1} (S2).Note that the corrected black curve in Figure 3c is significantly smoother than that in Figure 3a. For this interval at station B004, some of the signals that were uncorrectable in the original ε_{E-N} record simply do not appear or need to be corrected on the nonatmospheric component ε_{E-N-na}.

To see the noise reduction more systematically, we estimate the variance of the corrected strain data in the 6 h to 5 day band in 100 overlapping 100 day-long segments, spaced roughly every 30 days through the 9 years of data. Variances of the original and corrected data are shown in plots b and d of Figures 3, 4, supporting information Figures S1 and S2. For all 4 strain records, the average variance of the corrected nonatmospheric strains is smaller than the variance of the corrected original shear strain. In many cases, the variance of the corrected nonatmospheric strains is an order of magnitude smaller. This reduced noise level will be crucial for our analysis of RTRs in section 4, which produce strain signals not much larger than the noise.

3.4. Tidal and Diurnal Corrections

Once we have identified the weights required to avoid large atmospheric strains, we still have to remove the tides. We use the original, uncorrected data to construct the ε_{E-N-na} and ε_{2EN-na} records. Then we remove nontectonic signals as before. We remove the long-term trends by correcting for a constant, linear trend, and decaying exponential. Then we estimate the tidal and diurnal signals as shown in

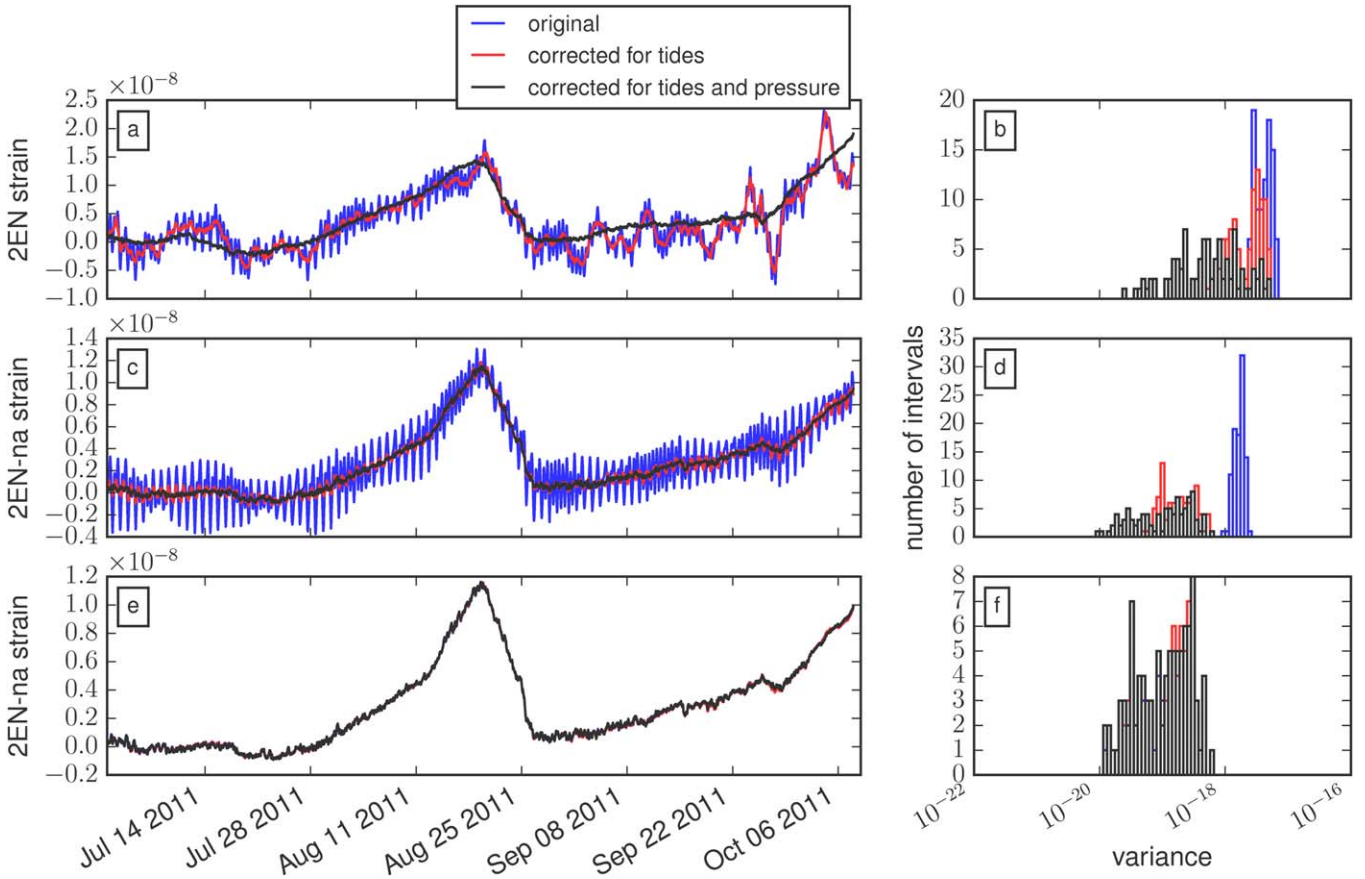

Figure 4. As in Figure 3, but for ε_{2EN} and ε_{2EN-na} at strainmeter B003.

equation (3), but omitting the now-unnecessary atmospheric correction. With the new strain components, the noise is significantly reduced, so we are able to compute the tidal corrections more precisely. We resolve and remove 23–49 tidal constituents rather than 8–21 constituents as in the original fits (supporting information Table S1). The estimated diurnal coefficients are shown in supporting information Figures S3 and S4. To check that these tidal and diurnal corrections are sufficient—that no further time-dependent corrections are needed—we attempt to correct the corrected data in 100 day intervals. The variance distributions obtained with these 100-day corrections are shown in plot f of Figures 3, 4, and supporting information Figures S1 and S2. The additional variance reduction from further time-dependent corrections is small, of order 10%, and we choose not to pursue those corrections for this study. To obtain the strain data used to examine RTRs, we estimate a single correction by fitting equation (3) to the entire 9-year strain record.

4. Changes in Strain Rate Associated With RTRs

4.1. Interpreting Strain Rate in Terms of Moment Rate

We use the corrected strain data to look for variations in strain rate associated with tremor reversals. Assuming slip occurs exclusively on the plate interface, the strain rate can vary for two reasons: because the moment rate changes or because the dominant location of slip changes. The effect of the migrating slip location can be seen in Figure 5a, where the ε_{E-N} strain rate changes sign as the slow slip event propagates past strainmeter B004, as well as in supporting information Figures S5–S8. Models of the migrating 50–75 km wide slow slip events reproduce those strain observations reasonably well [*Dragert and Wang*, 2011; *Roeloffs*, 2015; *Krogstad and Schmidt*, 2015]. Models of spatial variation in slip on the 10–20 km RTR length scales have been less well tested. The strain Green's functions can vary strongly over 20 km, as this distance is a significant fraction of the 30–50 km depth of slip and the 50–100 km horizontal distance from the slip

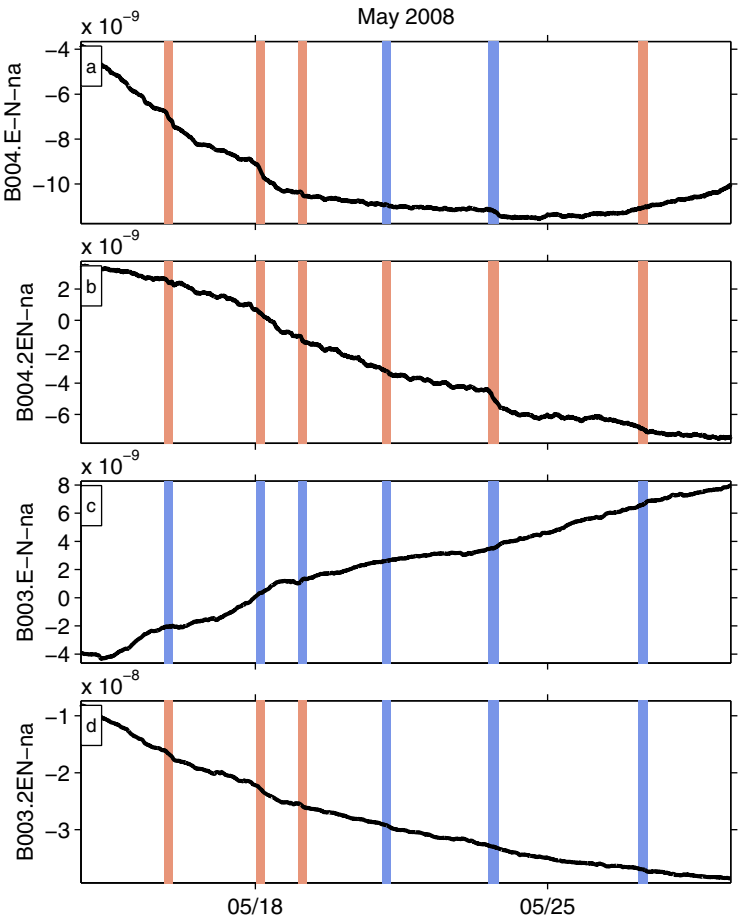

Figure 5. Strain observed during part of the May 2008 slow slip event. A longer record is shown in supporting information Figure S5. Bars indicate the times of tremor reversals. Red bars mark RTRs where a 150% rate increase during the RTR would be resolvable with 70% probability, according to the uncertainty estimates from section 4.3. Blue bars mark RTRs where a 150% rate change would not be resolvable.

location to the strainmeters (see supporting information Figure S13). As discussed in supporting information section S6, uncertainties in slip location, interface dip, elasticity structure, and strainmeter calibration can lead to significant uncertainties in the Green's functions for an individual RTR.

Because of these uncertainties, we choose not to use calculated Green's functions in our primary forward model. Instead, we simplistically assume that the RTR Green's functions are the same as the Green's functions for a nearby 3 day interval of slow slip. In other words, we assume that the location of slip is constant on timescales of 3 days, and during the RTRs. With this assumption, we can interpret any fractional increases in strain rate during RTRs as fractional increases in moment rate.

The calculations in supporting information section S6 suggest that the RTR Green's functions sometimes differ from a 3 day average Green's functions by a factor of a few (see supporting information Figures S15 and S16). In a few cases, when the strainmeter is near a nodal plane, the Green's functions can vary more strongly, even changing sign. This uncertainty in the Green's functions suggests that we should not overinterpret any individual RTR moment rate estimate. Instead, we consider the ensemble of estimated RTR moment rates.

In calculating the variations in the strain Green's function, we assume along-dip slip on the plate interface model of *McCrory et al*. [2012]. But the Green's function could also change if the orientation of slip in RTRs differs from that of the main slow slip event. The locations and focal mechanisms of slow slip, tremor, LFEs, and very low-frequency earthquakes (VLFEs) in Cascadia are mostly found to be consistent with shear slip on the plate interface, either in the pure dip-slip direction or in the plate motion direction [*Wech and Creager*, 2007; *Szeliga et al*., 2008; *Brown et al*., 2009; *Wech et al*., 2009; *Schmidt and Gao*, 2010; *Bartlow et al*., 2011; *Royer and Bostock*, 2014; *Ghosh et al*., 2015; *Hutchison and Ghosh*, 2016].As discussed in supporting information section S6, small variations in the slip rake—from pure thrust to the plate motion direction—are unlikely to influence the bulk of the RTR observations. However, we note that a few LFEs may have different, more strike-slip focal mechanisms [*Royer and Bostock*, 2014], and tremor is sometimes inferred to be more distributed in the overriding plate [*Kao et al*., 2005, 2009]. If a few RTRs also consist of slip on a different fault plane, they could have different Green's functions and produce very different surface strains. These potential outliers again encourage us to interpret only the median RTR behavior. As we do so, we will assume that most RTRs occur on the plate interface, with roughly dip-slip motion.

Even when considering the ensemble of measurements and assuming that RTRs occur on the plate interface, we must note one persistent trend in the slow slip Green's functions. The RTR regions tend to have larger-amplitude Green's functions than the 3 day-averaged slow slip regions. The difference arises mostly because the static strain field decays with distance from the slip locations, and the RTR areas are concentrated in the updip half of the slow slip region, closer to the strainmeters. The larger RTR Green's functions suggest that we may overestimate the RTR moments by a factor of approximately 1.3 when we interpret all variations in strain rate as variations in moment rate. We will recall this moment uncertainty in the discussion in section 5. In the next section, we simply estimate the change in strain rate during RTRs.

4.2. Quantifying Strain Rate Changes

A visual inspection of the slow slip strain reveals increased strain rates during a number of reversals, consistent with increased moment rates (blue and red bars in Figure 5, supporting information Figures S10–S12). The observed strain rate changes are not much larger than the noise, however, so we need to quantify these increases and check that they are systematic—unlikely to occur by chance.

To isolate any strain rate changes, we compare the average strain rate during each RTR with three estimates of the background strain rate, representative of the slow slip moment rate on a 3 day timescale. Our first and primary estimate of the background rate is the average strain rate during the 3 days centered on the RTR time. We subtract this background rate from the RTR strain rate to determine the RTR strain rate change. Then we divide the RTR strain rate change by the 3 day background rate to obtain the fractional strain rate change during RTRs.

We do a similar difference and normalization with the second background rate estimate. The second background rate is also the average strain rate during the three days centered on the RTRs, but this time excluding all RTR intervals. This non-RTR background rate could differ from the simple 3 day average if the RTRs account for a large fraction of the slow slip moment.

These two background rate estimates seem reasonable approximations of the average strain rate surrounding RTRs, and we always subtract one of them from the RTR strain rate to isolate the RTR strain rate change. However, these background rates might be less appropriate for normalizing to the fractional rate change. RTRs rupture back through a region that has already slipped, not ahead of the front, so the strain rate observed before the RTRs may provide a better estimate of the relevant normalization. Thus we also consider a third background strain rate estimate: the average strain rate in the 3 days prior to the reversals.

All of the background strain rates, as well as the strain rate during the RTR, are computed by drawing a line through the first and last points in the intervals of interest. Such a rate estimate is appropriate when the noise is characterized by a random walk, as seems a reasonable approximation for the strain data in the frequency range of interest [e.g., *Langbein*, 2004, 2010; *Hawthorne and Rubin*, 2013b].

We calculate the background-normalized RTR strain rate change for observations of each reversal at each station and component. Histograms of the well-constrained strain rate changes are shown in Figure 6.

4.3. Uncertainty-Based Data Selection

Only about 60 of the 124 estimated strain rate changes are shown in the distributions in Figure 6 because in many cases, the RTR strain rate change is poorly constrained by the observations. The allowable resolution varies among the strain records because some of the reversals occur when the background strain rate is low. When the background strain rate is small, a 100% increase in strain rate is also small, and often unresolvable.

To determine if changes in strain rate should be resolvable for a given RTR, we consider realizations of the noise from data outside slow slip events. We examine 3000 times away from slow slip events and extract two strain rates for each one: a short-term rate, taken from an interval with duration equal to the RTR, and a long-term rate, taken from a 3 day interval centered on or immediately before the short-term interval.

We use these 3000 strain rate pairs to determine if the RTR observation passes two uncertainty criteria. The criteria are chosen to identify a cluster of observations that have roughly similar uncertainties, so that we still have a representative sample of the average behavior of RTRs, but we exclude observations that provide little additional information about RTR strain rate changes. In our first criterion, we examine whether

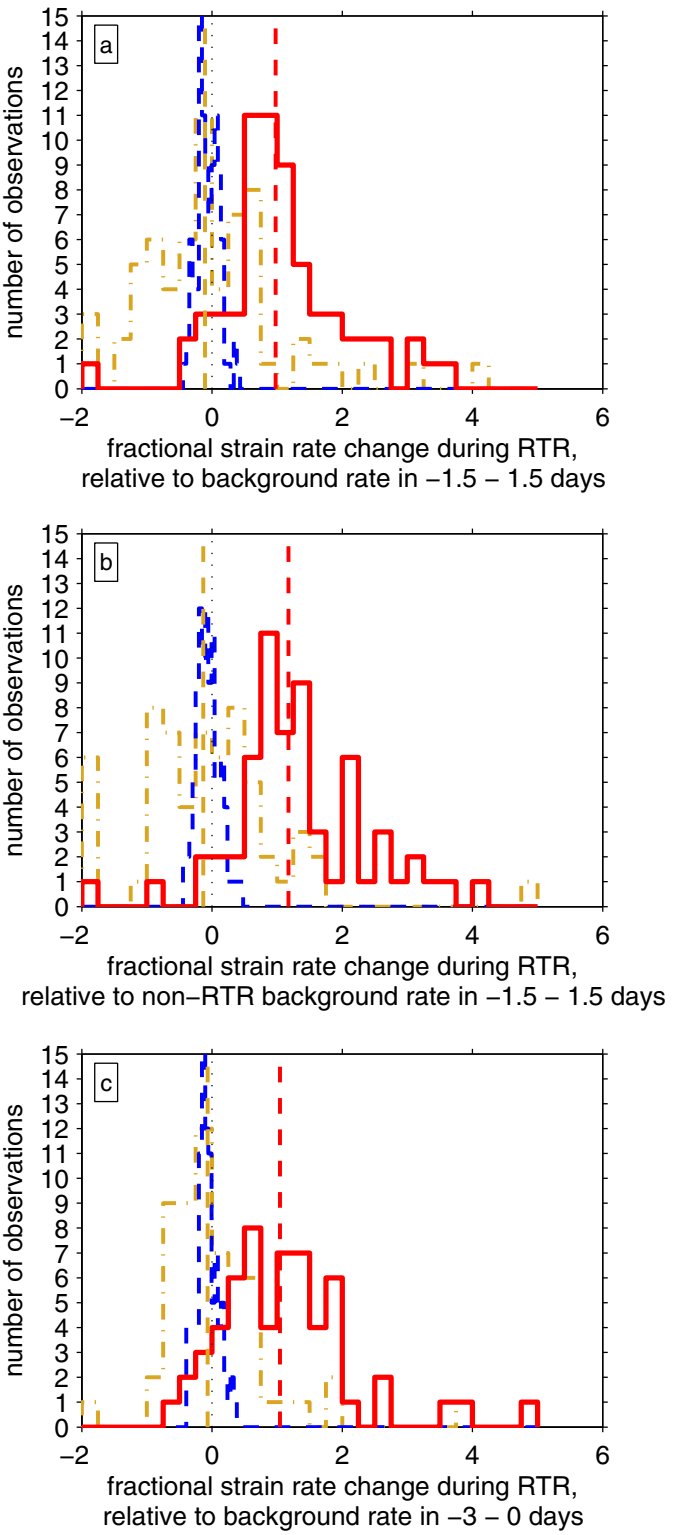

Figure 6. In all plots, solid red lines show the distribution of fractional strain rate changes during all RTR observations with acceptable uncertainties. Vertical-dashed red lines show the median rate changes. Dashed-dotted yellow lines show one set of strain rate changes obtained by time-shifting all the RTRs. Vertical-dashed yellow lines shows the median of those changes. Blue-dashed lines indicate the median rate changes for 100 different time shifts. These values are all smaller than the median estimated during RTRs (vertical red-dashed line). The background strain rate estimates differ among the plots. The background rates are estimated (a) as the average strain rates in 3 day intervals centered on the RTR, (b) as the average strain rates in 3 day intervals centered on the RTR, but excluding the RTR times, or (c) as the average strain rates in 3 day intervals before the RTR. Note that the handful of values smaller than −2 are placed in the leftmost bin.

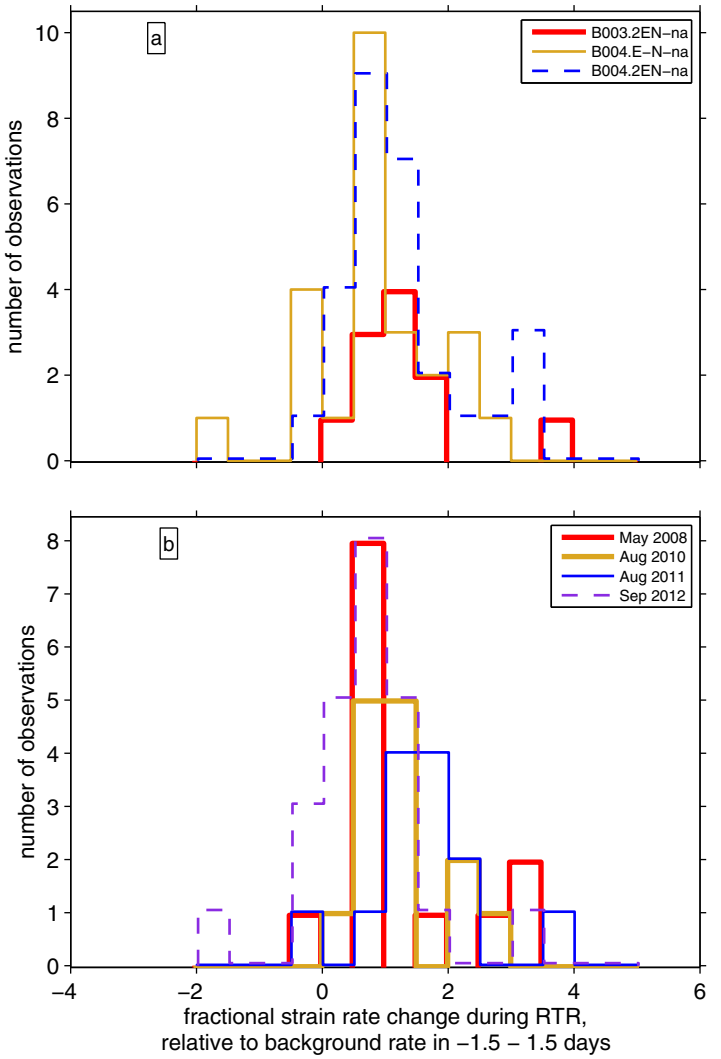

Figure 7. Histograms of RTR strain rate changes obtained at (a) various stations and components and (b) during the different slow slip events. The histogram outlines have been shifted slightly so that they do not plot on top of each other.

the background strain rate estimated during the slow slip event is well resolved. We throw away any RTR observations where fewer than 70% of the long-term strain rates are smaller than 0.75 times the background strain rate. In our second criterion, we examine whether fractional strain rate changes should be resolvable. We compute the ratios of the short-term strain rates to the summed RTR background rate and long-term strain rates, and take these ratios as estimates of the uncertainties on the fractional strain rate change. We throw away observations where fewer than 70% of the ratios have amplitudes smaller than 1.5. This leaves us with about 60 RTR observations where a 150% change in strain rate would be significant with at least 70% probability.

Note that while the uncertainty estimates and data selection use the 3 day background strain rates, they do not use the RTR strain rates. Our data selection is therefore unbiased by the RTR strain rates. If there is bias, it is likely toward selecting intervals with anomalously high background strain rates, as a higher-than-actual background rate would lead to a lower-than-actual uncertainty. Higher-than-actual background rates would lead us to underestimate the strain rate changes in RTRs.

4.4. Results

The fractional RTR strain rate changes observed in the $\approx$ 60 well-resolved RTR intervals are dominantly positive, as shown in the distributions in Figure 6. The median strain rate increase is roughly 100% for all three estimates of the background strain rate (different plots of Figure 6). For the primary background strain rate (Figure 6a), the median fractional rate increase is 1.0 (a 100% increase), and 52 of the 64 of the values are larger than 0.5. Interpreted simply, these strain rate increases imply that, on average, the moment rate increases by 100% during RTRs. Note that the scatter in the estimated strain rate changes may or may not result from real variations in RTR moment; as noted above, we include individual rate increases even if the 70% uncertainty is as much as a factor of 1.5, or 150%.

The strain rate increases persist over the two stations and four slow slip events. Histograms of rate changes divided by station and event, shown in Figure 7, all imply a roughly 100% strain rate increase during the reversals.

To further confirm that the observed strain rate increases are unlikely to occur by chance, we consider the rates obtained at alternative times within slow slip events. We take the RTRs and move them all by a common time shift: by a random amount between 0.5 and 3 days forward or backward. We then complete the RTR rate estimation as if these were the appropriate times. We choose to shift all RTRs by the same amount because some of the noise is tidal or diurnal, and it might affect multiple reversals similarly. The dashed-dotted yellow lines in Figure 6 show the fractional strain rate changes obtained from one time shift. As expected, the values are scattered but centered at 0. The median strain rate change is −0.1 (yellow-dashed vertical lines). Median rate changes obtained for 100 random time shifts are illustrated with the blue-dashed histograms in Figure 6. 90% of the 100 median rate changes have amplitudes smaller than 0.3. None of the medians reach a 100% increase in strain rate, as observed at the RTR times. These median non-RTR strain rate changes provide one estimate of uncertainty on the median RTR strain rate increase. They suggest that noise in the data introduces a 30% uncertainty on the 100% median strain rate increase.

5. Implied Moments, Slips, and Stress Drops

5.1. Interpreting Relative Strain Rate as Relative Moment Rate

The simplest interpretation of the observed 100% strain rate increase is that the slow slip moment rate increases by 100% ± 30% during RTRs, where the range indicates the 90% confidence interval associated with noise in the data. In making this interpretation, however, we are assuming that the Green's function does not change significantly with the changing location of slip during tremor reversals. As noted in section 4.1, our interpretation of the strain rate change could be influenced by uncertainties in the Green's functions or in the location of slip in the RTRs. Along-strike migration of slip can increase or decrease the Green's functions, so along-strike location changes are not expected to introduce a systematic bias. But updip migration of the slip, to locations closer to the strainmeters, tends to increase the amplitude of the strain Green's functions. Such migration could explain part of the observed increase in strain rate. We calculate that if all of the slip moved to the uppermost 25% of the slow slip region but stayed at the same location along strike as the RTRs, the median Green's function amplitudes would increase by about 30%.

In sections 4.1 and supporting information Figure S6, we calculate the Green's functions for 3 day average slow slip regions as well as for the specific RTR regions used. We note that these Green's functions sometimes differ by a factor of a few and that there is a tendency for the RTR regions to produce larger strain per moment than the nearby slow slip regions. The median difference is modest, less than a factor of 1.3. Nevertheless, these Green's functions suggest that we could be overestimating the change in moment rate associated with RTRs by around a factor of 1.3 when we interpret fractional strain rate changes as fractional moment rate changes. Indeed, when we incorporate the calculated RTR Green's functions into our moment rate calculations in supporting information section S6, we estimate a median moment rate increase of 75% ± 25% rather than 100% ± 30% (supporting information Figure S17). Combining these ranges gives a 90% confidence interval on the moment rate between 50 and 130%.

5.2. Moment

The estimated 50–130% median moment rate increases are averaged over the 2–7 h-long RTRs. To compute the total moment associated with each RTR, we multiply the moment rate increases by the RTR durations and plot the resulting moments in Figure 8a. There are a handful of negative RTR moments, estimated when the strain rate decreases during the RTR. These are plotted in the gray region below the break in scale in Figure 8a. But 54 of the 60 moment estimates are positive. The median RTR moment is 16% ± 5% of the moment in 1 day of slow slip when we assume the same Green's functions in the RTR and larger-scale slow slip regions. The quoted error bars on the median are mapped from the 30% uncertainty on the median strain rate increase obtained in section 4.4. If the Green's functions are a factor of 1.3 larger in the RTR region, the estimated RTR moments will be a factor of 1.3 smaller, giving median moment 11% ± 3% of the daily slow slip moment. Note that the uncertainty in each individual moment estimate is large, so the scatter in the calculated RTR moments could be due to noise.

To convert the fractional moments to absolute RTR moments, we multiply by the daily moment in a slow slip event. As a rough estimate of the daily slow slip moment, we take the moment of a typical M_W 6.6 slow slip event and divide by a typical duration of 30 days, to get the equivalent of a M_W 5.6 earthquake [e.g., *Szeliga et al.*, 2008; *Wech et al.*, 2009; *Schmidt and Gao*, 2010; *Gao et al.*, 2012]. The implied RTR moments are

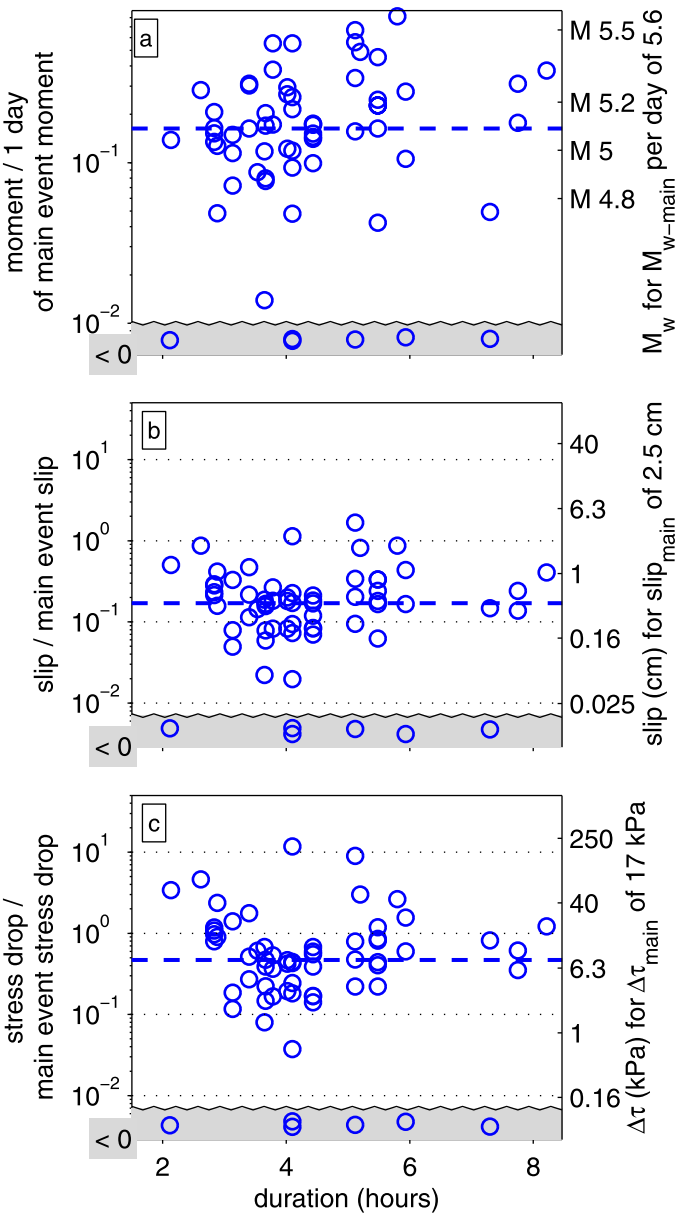

Figure 8. (a) Estimated moment in each RTR, as a fraction of the moment in 1 day of slow slip. The right hand axis shows the absolute moment implied if the moment in 1 day of slow slip is equivalent to a M_W 5.6 earthquake. (b) Estimated peak slip in each RTR, as a fraction of the peak slip in the slow slip event (left hand axis) and in absolute terms (right hand axis). (c) Estimated stress drop in each RTR, as a fraction of the stress drop in the slow slip event (left hand axis) and in absolute terms (right hand axis). The slip and stress drop estimates assume uniform stress drop over the rectangular regions identified in section 2. For all plots, negative values—those predicted by decreases in strain rate—are plotted along a line below the break in scale, with vertical offsets used only to distinguish multiple observations of a given RTR.

plotted on the right hand axis of Figure 8 and imply a median equivalent magnitude of M_W 5.1 when the Green's functions are assumed to be uniform and a median equivalent magnitude around M_W 5.0 when the Green's functions are assumed to be a factor of 1.3 larger in the RTR region.

These moments suggest that RTRs could accommodate a significant fraction of the slow slip moment. If RTRs with equivalent magnitudes around M_W 5.1 occur of order once per day, as seen in the tremor observations [*Royer et al.*, 2015], RTRs might release 10% of the slow slip moment beneath southern Vancouver Island. We can better quantify this estimate of the total RTR moment release with a slightly different analysis. In Figure 9, we compare 2 versions of the 3 day background strain rates: the simple 3 day averages and the 3 day averages excluding RTRs. If most of the slip occurred during reversals, we would expect the average strain rate to decrease when we exclude the RTR intervals. We find that the strain rate is about 10% smaller when the RTR times are excluded. The 10% strain rate decrease suggests that of order 10% of the slow slip moment is accommodated by tremor reversals. The percentage is likely underestimated, however, as not all RTRs have been identified. If half of the RTRs remain undetected, of order 20% of the slow slip moment could accumulate in RTRs.

5.3. Slip

If we assume that moment in RTRs accumulates in the regions that generate propagating tremor, we can determine additional properties of the reversals, such as their slips, slip rates, and stress drops. In order to determine the slips, we first convert the absolute moments estimated above to potency assuming a shear modulus of 30 GPa, as commonly used in geodetic slip inversions. Then we assume that the slip associated with each RTR accumulates in a rectangular region defined by the LFE locations, as identified in section 2. The stress drop in this rectangular region is assumed to be uniform. The slip is assumed to vary smoothly with location to match the uniform stress distribution. We then scale this slip distribution so that it would produce the estimated potency and extract the peak slip value. The obtained peak slips are shown with the right hand axis in Figure 8b. The

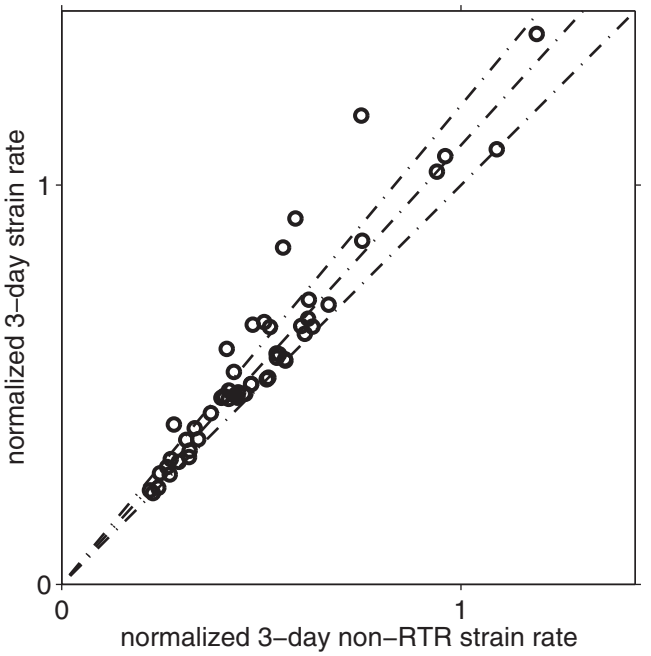

Figure 9. Three day average strain rate compared with the 3 day average excluding intervals with RTRs. For plotting purposes, rates are normalized by the strain rate within the RTR at the center of each 3 day average. The 3 day strain rates are mostly a few to 20% higher when the RTRs are included, suggesting that of order 10% of the slow slip moment is accommodated by the identified RTRs. Dashed lines have slopes of 1, 1.1, and 1.2.

median peak slip is 0.44 ±0.13 cm when we assume no change in the Green's function during RTRs and 0.36 ±0.11 cm when we account for the changing Green's functions (supporting information Figure S18b), where the uncertainties account only for noise in the data.

For comparison, we estimate the peak slip in the overall slow slip event. A M_W 6.6 slow slip event that extends 300 km along strike and 60 km along dip with uniform stress drop would have peak slip of 2.5 cm, roughly 5 to 10 times larger than the slip in an RTR.

As we estimate slip we must consider a second source of uncertainty: the spatial extent of the RTR and slow slip regions. For instance, if the main event has an along-dip width of 50 or 75 km, not 60 km as we have assumed, the main event peak slip will be 20% larger or smaller. Observed along-dip tremor extents are mostly between 50 and 60 km [e.g., *Wech et al*., 2009; *Houston et al*., 2011; *Bostock et al*., 2012; *Armbruster et al*., 2014; *Royer and Bostock*, 2014; *Boyarko et al*., 2015], while geodetic along-dip extents reach about 75 km [*Szeliga et al*., 2008; *Wech et al*., 2009; *Schmidt and Gao*, 2010]. Similarly, if the lengths and widths of the RTRs are a factor of 1.4 larger or smaller than we have estimated, as would seem a limiting scenario for most RTRs given the tremor locations [*Royer et al*., 2015 and see supporting information Figures S19–S52], the RTR peak slips will be a factor of 2 smaller or larger.

Even with these uncertainties, we can consider the ratio of the slip in RTRs relative to the total slip in the slow slip event. The estimated ratios of main event slip to RTR slip—between 5 and 10—would suggest that at most locations, most of the slip occurs outside of RTRs. However, RTRs are not evenly distributed throughout the slow slip region; they appear to be more common in the updip areas. In Figure 10, we have summed the expected slip accumulated in RTRs in each slow slip event, normalized by the median peak slip obtained from the RTRs. For this calculation, we use the boxes chosen from the LFE locations and assume slip distributions corresponding to a uniform stress drops in each RTR. Some locations appear to rupture in three or more RTRs per slow slip event and may accumulate more than half the total slip in the slow slip event during RTRs. The color bar in Figure 10 is marked with the fraction of slip that would be accommodated by RTRs if the peak slip in each RTR accommodates one-sixth of the total slip.

The RTR slips computed here are larger than those obtained by *Royer et al*. [2015]. *Royer et al*. [2015] estimated that, on average, 7% of detected LFEs occurred within RTRs. However, many of the LFE families were in locations with few or no RTRs. In some LFE families, RTRs contained 30% of the LFEs. If the LFE rate is proportional to slip, such a percentage would suggest that, on average, about 30% of slip at those locations occurs in RTRs. Our best estimates give slightly larger RTR slip percentages, often around 50%, in a slightly larger area, though still in the updip region beneath Vancouver Island (see Figure 10) [*Houston et al*., 2011; *Y. Peng et al*., 2015; *Royer et al*., 2015].

Our larger slip estimates could be partially explained if the lower range of our RTR slip estimates are correct—if the larger slip estimates suffer from underestimated RTR Green's functions. In addition, we should note that the LFE slip estimates use the rough assumption that slip rate is proportional to LFE rate [*Royer et al*., 2015]. If the ratio of slip rate to LFE rate is higher during RTRs, the fractional RTR slip estimated from

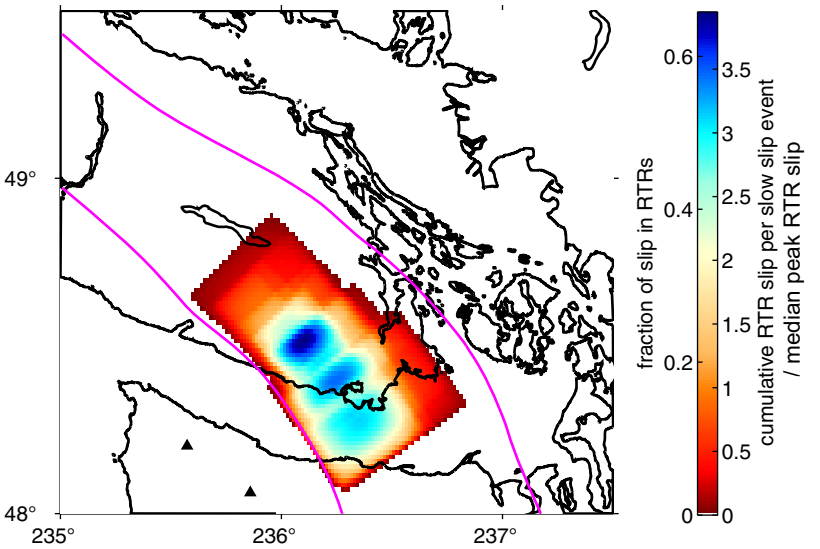

Figure 10. Cumulative slip in RTRs per slow slip event, as a fraction of the peak slip in the median RTR. Each RTR is assumed to slip over the areas identified in section 2 and shown in supporting information Figures S19–S52. The left hand axis of the color bar shows the fraction of the total slip in the slow slip event that would be accommodated by RTRs if each RTR had peak slip one-sixth of the total slip in the slow slip event.

LFEs should be increased from that of *Royer et al.* [2015]. Such an increase in slip per LFE may be suggested by the larger LFE moments observed during tremor reversals [*Rubin and Armbruster*, 2013; *Bostock et al.*, 2015; *Peng and Rubin*, 2016] and, albeit with more ambiguity, by the increase in overall amplitude of tremor during RTRs [*Thomas et al.*, 2013].

5.4. Slip Rate

Given the RTR and main event slips, we can estimate slip rates. A given LFE family generates most of its RTR-related events over about 2 h [*Royer et al.*, 2015]. If one location in an RTR accumulates 0.4 cm of slip over 2 h, as estimated in section 5.3, average RTR slip rates would be roughly 0.8 μm/s. Using a smaller slip estimate of 0.3 cm, closer to the median computed with differentiated RTR Green's functions, gives a median RTR slip rate of 0.6 μm/s. Both of these slip estimates also suffer from 30% uncertainty in the data, as well as assumptions about the slip distribution in RTRs.

For comparison, most tremor in the main slow slip front occurs over 1 to 2 days, within a roughly 10 km region [*Wech and Creager*, 2008; *Ghosh et al.*, 2010b; *Royer et al.*, 2015; *Bostock et al.*, 2015; *Peng and Rubin*, 2016]. 2.5 cm of slip during a one to 2 day period suggests average slip rates of 0.1 to 0.2 μm/s, a factor of a few to 10 smaller than slip rates estimated for RTRs. At locations where more than half the total slip accumulates during RTRs, the slip rate outside of reversals could be a further factor of 2 lower.

5.5. Stress Drop

5.5.1. Assuming Uniform Stress Drop

We also calculate the stress drops associated with the slip distributions obtained in section 5.3, again assuming rectangular regions of uniform stress drop for both the RTRs and main slow slip event. We assume a shear modulus of 30 GPa, as above. The stress drops obtained for individual observations are plotted in Figure 8c. The median stress drop is 8 ± 2.5 kPa assuming uniform Green's functions and as low as 6 ± 2 kPa assuming larger Green's functions in the slow slip region. Both estimates are roughly 50% of the 17 kPa main event stress drop obtained for a uniform stress drop event with 60 km along dip width and 2.5 cm peak slip.

We have assumed a 30 GPa shear modulus for these stress drop estimates as representative of the average large-scale stiffness of the crust in the slow slip region. However, the rigidity of the rocks in the several kilometers below the plate interface in the slow slip region is likely lower. An 18 GPa shear modulus is more consistent with these local seismic velocity estimates [*Audet et al.*, 2009; *Hansen et al.*, 2012; *Nowack and Bostock*, 2013; *Royer et al.*, 2015]. Such a locally low rigidity seems unlikely to control the strain observed at

the surface, but for completeness we note that if we did assume a shear modulus of 18 GPa, both the RTR and main event stress drop estimates would be a factor of 1.5 smaller, giving an RTR stress drop around 5 kPa.

Uncertainty in the RTR Green's functions again introduces a potential error, making it possible that the actual RTR stress drops are a factor of 1.3 smaller than our estimates. And as we move from estimating slip to estimating stress drop, we introduce more uncertainty from potential errors in the spatial extents of RTRs. If both dimensions of RTRs are a factor of 1.4 smaller than our estimates, the stress drops would be a factor of 3 larger, with median 1.5 times the main event stress drop. Or, as seems slightly more plausible given the tremor locations, if both RTR dimensions were a factor of 1.4 larger than our estimates, the RTR stress drops would be a factor of 3 smaller, with median 0.15 times the main event stress drop.

5.5.2. From Slip Accumulated Behind the Front

We may also estimate RTR stress drops by considering the kinematics of slip accumulation during propagation. As the RTR propagates, slip likely accumulates most rapidly near the tip of the moving front. LFE detection rates are typically highest within a 10 km portion of the RTR, with each LFE location displaying high detection rates for about 2 h [*Royer et al*., 2015]. We refer to the length of this 10 km region of rapid slip as L_1, and assume that a slip δ accumulates within it.

Slip δ occurring over a distance L_1 results in a stress drop $\Delta\tau$ of

$$\Delta\tau = \alpha\mu\frac{\delta}{L_1}. \tag{6}$$

Here α is a factor of order 1 accounting for the geometry of the front. $\alpha = 1/\pi$ if the stress drop is uniform within L_1 of the front, if slip is uniform farther than L_1 from the front, and, most importantly for us, if the along-dip width W is much longer than the along-strike length of slip accumulation L_1 [*Rubin and Ampuero*, 2009]. For our RTRs, with along-dip width W of 20–30 km, α is likely about a factor of 1.5–2 larger, around 0.6, as calculated in supporting information section S8. Assuming this geometry factor and a slip of 0.4 cm, we obtain a stress drop of 7 kPa, similar to the 8 kPa median obtained in section 5.5.1. Note, however, that we obtained the median stress drop here using the same slip used for the stress drops in section 5.5.1, so it would be surprising if the estimated stress drops were very different.

We can also calculate the stress drop of the main slow slip event using propagation arguments. The main event has a region of rapid tremor accumulation of 10–20 km, but a longer along-dip width, so a geometric factor α of $1/\pi$ is more appropriate. For a peak slip of 2.5 cm, the main event stress drop is between 13 and 25 kPa, again similar to the values obtained in section 5.5.1.

Finally, we can compare our 7 kPa stress drop with the 0.8 kPa stress drop obtained from LFEs by *Royer et al*. [2015]. Of the factor of 9 difference in these two estimates, a factor of 1.5 results from the different shear moduli used: 30 GPa versus 18 GPa. Most of the remaining difference arises because we estimate that each RTR has slip around one-sixth of the main event slip, while *Royer et al*. [2015] take an average of all LFE families and assume that each RTR has slip around 7% of the main event slip. The rest of the difference arises only because *Royer et al*. [2015] assumed infinite along-dip widths in their stress drop estimates. They chose $\alpha = 1/\pi$, while we chose $\alpha = 0.6$.

6. Discussion

Our analysis of the strain and tremor data suggest that RTRs accommodate a significant but not dominant portion of the slow slip moment release. The observed strain rate changes imply a median moment per RTR between 8 and 21% of the moment in one day of slow slip, comparable to a M_W 5.0 or 5.1 earthquake. If RTRs occur at a rate around once per day, RTRs as a whole could release 10–20% of the slow slip moment in the Vancouver Island region.

Coupling the RTR moments with tremor locations suggests a median peak slip per RTR of 0.4 cm, 20% of the main event slip; a median near-front slip rate of 0.8 μm/s, about 6 times the main event slip rate; and a median stress drop of 8 kPa, 50% of the main event stress drop. While all of these properties—moment, slip, slip rate, and stress drop—have a factor of a few uncertainty derived from the data, Green's functions, and RTR areas, they nevertheless provide order of magnitude constraints for modeling RTRs.

6.1. RTR Propagation Rates

One purpose of constraining the properties of RTRs is to understand why RTRs propagate rapidly—10–40 times faster than the main front [*Obara*, 2010; *Houston et al*., 2011; *Royer et al*., 2015; *Y. Peng et al*., 2015]. In section 5.5.2 (equation (6)), we described the elasticity constraints on slip δ accumulating in a propagating front, within a distance L_1 of the tip. If we assume that this slip accumulates over a time Δt, it becomes clear that elasticity also constrains the average slip rate $V_{slip}=\delta/\Delta t$ and the propagation rate $V_{prop}=L_1/\Delta t$, leading to equation (1) [e.g., *Rubin and Ampuero*, 2005; *Shibazaki and Shimamoto*, 2007; *Rubin and Armbruster*, 2013]:

$$V_{prop}=\alpha V_{slip}\frac{\mu}{\Delta\tau}.$$

In this context, our observations suggest that RTRs propagate faster than the main front because (1) the slip rates are a factor of a few to 10 times larger, (2) the geometric factor α is a factor of 1.5 to 2 larger because of the smaller along-dip widths, and (3) the stress drops are roughly a factor of 2 smaller.

6.2. RTR Strain Energies

If we are to understand why RTRs have higher slip rates but lower stress drops than the main front, it may be useful to consider the energy balance during RTR propagation. As an RTR ruptures into a region that is slipping slowly, it creates high stresses at the propagating edge. When the near-tip regions slip at these high stresses, energy is dissipated. The fracture energy G_c expended per unit propagation is supplied by an equivalent release of stored strain energy G in the RTR region.

The allowable strain energy release rate G is a function of the stress drop $\Delta\tau$ and the area of the event. For both the main slow slip event and the RTRs, the strain energy release rate G should scale roughly as $\Delta\tau^2 W/\mu$. The along-strike length L is less important because it is usually significantly larger than the along-dip width W [e.g. *Lawn*, 1993; *Hawthorne and Rubin*, 2013c], though the strain energy G of some RTRs may be somewhat reduced relative to the estimate that scales as $\Delta\tau^2 W/\mu$ if they have lengths comparable to or smaller than their widths. Inserting numbers into the estimate $\Delta\tau^2 W/\mu$ thus gives us a slight overestimate of the ratio of the RTR strain energy to the main front strain energy. RTRs appear to have stress drops $\Delta\tau$ about half of the main front $\Delta\tau$ and along-dip distances W one-third to one-half of the main front W, suggesting that the strain energy release G should be about one tenth that of the main front.

The strain energy G must equal the fracture energy G_c, and so G_c should also be one order of magnitude smaller for RTRs. In most frictional models, the fracture energy is an increasing function of two parameters: the slip rate and the initial state of the fault, where the initial state parameterizes how well healed the fault is [e.g., *Rubin and Ampuero*, 2005; *Ampuero and Rubin*, 2008; *Liu and Rubin*, 2010; *Hawthorne and Rubin*, 2013c]. Given the high estimated slip rates during RTRs, we may then qualitatively imagine that RTRs can propagate with modest strain energy release because the fault is less well healed after the main front has passed, and thus can be ruptured with a lower fracture energy. Quantitatively, it may not be trivial to achieve an order of magnitude reduction in fracture energy in models of slow slip. In some frictional models chosen for slow slip, the effective fracture energy often depends strongly on slip rate, with a less pronounced dependence on initial conditions. So in the models, changing how well healed the fault is may minimally affect the fracture energy if the slip rate is fixed and high [*Shibazaki and Shimamoto*, 2007; *Liu and Rubin*, 2010; *Segall et al*., 2010; *Hawthorne and Rubin*, 2013c]. The strong dependence of the fracture on slip rate but not initial state helps to reproduce the limited range of daily-averaged slip rates seen throughout and between slow slip events, but it typically does not lead to rapid slip rates with modest strain energy release [*Rubin*, 2011; *Hawthorne and Rubin*, 2013a].

6.3. Along-Dip Variation in RTR Importance

The rapid slip rates in RTRs could be facilitated not just by time-dependent variations in fault healing, but also by spatial variations in fault properties, as suggested in the models of *Ando et al*. [2010], *Luo and Ampuero* [2011], and *Ando et al*. [2012]. Within the area studied here, RTRs appear to be more common in the updip half of the slow slip region. Our calculations sometimes suggest that RTRs could accommodate more than half of the slip in regions that experience at least 3 RTRs per event. It may be that these locations have different frictional parameters that facilitate rapid slip with low stress drops and fracture energies. For instance, reduced effective normal stresses or smaller evolution effect coefficients could lead to smaller

fracture energy for the same slip rate [e.g., *Rubin and Ampuero*, 2005; *Ampuero and Rubin*, 2008; *Liu and Rubin*, 2010; *Hawthorne and Rubin*, 2013c].

However, choosing frictional parameters that would allow for the observed stress drop and slip rates in RTRs would not necessarily lead to a model that actually produced tremor reversals. Indeed, if the regions prone to RTRs do have lower normal stress and lower resistance to rupture, it is puzzling that these regions do not simply slip more as the main front passes through, and thus release all of the available stress drop before RTRs could occur. One option is that slip at asperities in the RTR-prone regions take longer to nucleate than slip on the rest of the fault [*Luo and Ampuero*, 2011], so that the stress drop occurs later. However, it is not clear whether such a delayed-slip model can reproduce RTRs that repeatedly rupture a single location or RTR regions that host significant tremor before and between RTRs, as are suggested by the data [*Obara*, 2010; *Houston et al*., 2011; *Royer et al*., 2015; *Y. Peng et al*., 2015].

6.4. RTR Driving Stress

We estimate that the stress drop in each RTR is around 8 kPa, roughly a factor of 2 smaller than the main event stress drop. If this local stress drop is not the result of delayed slip of certain parts of the fault, it may be that the fault is reloaded after the main front passes through. If the fault stops sliding abruptly after the main front passes, the continued slip at the main front, now farther along strike, will increase the stress in the region behind it. This stress increase could facilitate the stress drop in RTRs [*Ando et al*., 2012; *Hawthorne and Rubin*, 2013a].

Alternatively, part of the RTR stress drop could be provided by the tidal load. The peak to trough tidal shear stress changes are typically around 3 kPa [*Hawthorne and Rubin*, 2010; *Royer et al*., 2015], about one-third of the median RTR stress drop. However, the absolute RTR stress drop has at least a factor of 2 uncertainty, as the relevant shear modulus may be a factor of 1.5 lower than our assumed value (see section 5.5), and incorrect assumptions about the Green's functions may have caused us to overestimate the stress drop by a factor of 1.3 (see section 5.5). The tidal load is an appealing source of stress given the observed tidal triggering of RTRs [*Thomas et al*., 2013; *Royer et al*., 2015; *Peng and Rubin*, 2016] and tremor well behind the front [*Houston*, 2015; *Royer et al*., 2015]. We note, however, that the tidal load is cyclic. Any stress increase in one part of the tidal cycle is offset by a stress decrease later in the cycle. RTRs sometimes re-rupture a given region in subsequent tidal cycles [*Thomas et al*., 2013; *Royer et al*., 2015]. If the first of two such RTRs uses some of the available stress drop, the RTR in the next cycle will start from a smaller initial stress—unless the area is reloaded by a nontidal stress.

6.5. RTR Contribution to Tidal Modulation

Whether or not the tidal stress is a significant portion of the RTR stress drop, tidal stresses influence the timing of RTRs [*Thomas et al*., 2013; *Royer et al*., 2015; *Peng and Rubin*, 2016]. Roughly 70% of RTRs occur at times of larger-than-average updip shear stress [*Royer et al*., 2015]. Tides are also observed to modulate the total moment of slow slip. When modeled as a sinusoidal variation, the slow slip moment rate varies 25% above and below the mean rate in the 12.4 h tidal cycle [*Hawthorne and Rubin*, 2010]. To consider the RTR contribution to the overall tidal modulation of slow slip, we calculate that if the RTR occurrence rate also varied sinusoidally, it would have to vary 70% above and below the mean to allow 70% of RTRs to occur at a larger-than-average stress. Assuming RTRs contribute 10 to 20% of the total slip moment, as estimated in section 5.2, RTRs alone might then cause the slow slip moment rate to vary 7–15% around its mean, contributing half of the overall tidal modulation of slow slip.

7. Conclusions

Our observations of strain rate variations suggest that RTRs account for 10–20% of the slow slip moment release beneath southern Vancouver Island. We find that strain rates increase during RTRs, with a median strain rate increase around 100% $\pm$ 30% among the $\sim$60 RTR observations considered. Such a variation in strain rate suggests an increase in the slow slip moment rate of 100%, though this RTR moment rate may be overestimated by a factor of 1.3 because of uncertainty in the RTR Green's functions. We estimate that the median individual RTR examined releases moment between 8 and 21% of the moment released in 1 day of slow slip, equivalent to a M_W 5.0 or 5.1 earthquake. By assuming that this moment comes from a uniform stress drop rupture of the region that generates tremor in RTRs, we estimate a peak slip around

0.4 cm, between ten and a few tens of percent of the peak slip in the slow slip event; a near-front slip rate around 0.8 μm/s, between a few and 10 times the slip rate in the main front; a stress drop around 8 kPa, between 20% and comparable to the main event stress drop; and a strain energy release rate of order one-tenth that of the main front. With these RTR properties, we infer that the rapid propagation rates in RTRs result from both higher slip rates and decreased stress drops, but that RTRs reach these high slip rates with only modest strain energy release.

Acknowledgments
The strain data used comes from Plate Boundary Observatory stations, operated by UNAVCO for EarthScope and supported by the National Science Foundation EAR-0350028 and EAR-0732947. It can be obtained from UNAVCO via IRIS. We thank associate editor Heidi Houston, Abhijit Ghosh, and an anonymous reviewer for comments that improved the manuscript.

References

Ampuero, J.-P., and A. M. Rubin (2008), Earthquake nucleation on rate and state faults: Aging and slip laws, *J. Geophys. Res.*, *113*, B01302, doi:10.1029/2007JB005082.

Ando, R., R. Nakata, and T. Hori (2010), A slip pulse model with fault heterogeneity for low-frequency earthquakes and tremor along plate interfaces, *Geophys. Res. Lett.*, *37*, L10310, doi:10.1029/2010GL043056.

Ando, R., N. Takeda, and T. Yamashita (2012), Propagation dynamics of seismic and aseismic slip governed by fault heterogeneity and Newtonian rheology, *J. Geophys. Res.*, *117*, B11308, doi:10.1029/2012JB009532.

Armbruster, J. G., W.-Y. Kim, and A. M. Rubin (2014), Accurate tremor locations from coherent S and P waves, *J. Geophys. Res.*, *119*, 5000–5013, doi:10.1002/2014JB011133.

Audet, P., M. G. Bostock, N. I. Christensen, and S. M. Peacock (2009), Seismic evidence for overpressured subducted oceanic crust and megathrust fault sealing, *Nature*, *457*, 76–78, doi:10.1038/nature07650.

Bartlow, N. M., S. Miyazaki, A. M. Bradley, and P. Segall (2011), Space-time correlation of slip and tremor during the 2009 Cascadia slow slip event, *Geophys. Res. Lett.*, *38*, L18309, doi:10.1029/2011GL048714.

Bostock, M. G., A. A. Royer, E. H. Hearn, and S. M. Peacock (2012), Low frequency earthquakes below southern Vancouver Island, *Geochem. Geophys. Geosyst.*, *13*, Q11007, doi:10.1029/2012GC004391.

Bostock, M. G., A. M. Thomas, G. Savard, L. Chuang, and A. M. Rubin (2015), Magnitudes and moment-duration scaling of low-frequency earthquakes beneath southern Vancouver Island, *J. Geophys. Res.*, *120*, 6329–6350, doi:10.1002/2015JB012195.

Boyarko, D. C., M. R. Brudzinski, R. W. Porritt, R. M. Allen, and A. M. Tréhu (2015), Automated detection and location of tectonic tremor along the entire Cascadia margin from 2005 to 2011, *Earth Planet. Sci. Lett.*, *430*, 160–170, doi:10.1016/j.epsl.2015.06.026.

Brown, J. R., G. C. Beroza, S. Ide, K. Ohta, D. R. Shelly, S. Y. Schwartz, W. Rabbel, M. Thorwart, and H. Kao (2009), Deep low-frequency earthquakes in tremor localize to the plate interface in multiple subduction zones, *Geophys. Res. Lett.*, *36*, L19306, doi:10.1029/2009GL040027.

Cartwright, D. E., and A. C. Edden (1973), Corrected tables of tidal harmonics, *Geophys. J. Int.*, *33*(3), 253–264, doi:10.1111/j.1365-246X.1973.tb03420.x.

Cartwright, D. E., and R. J. Tayler (1971), New computations of the tide-generating potential, *Geophys. J. Int.*, *23*(1), 45–73, doi:10.1111/j.1365-246X.1971.tb01803.x.

Dragert, H., and K. Wang (2011), Temporal evolution of an episodic tremor and slip event along the northern Cascadia margin, *J. Geophys. Res.*, *116*, B12406, doi:10.1029/2011JB008609.

Dragert, H., K. L. Wang, and T. S. James (2001), A silent slip event on the deeper Cascadia subduction interface, *Science*, *292*(5521), 1525–1528, doi:10.1126/science.1060152.

Frank, W. B., N. M. Shapiro, A. L. Husker, V. Kostoglodov, A. Romanenko, and M. Campillo (2014), Using systematically characterized low-frequency earthquakes as a fault probe in Guerrero, Mexico, *J. Geophys. Res.*, *119*, 7686–7700, doi:10.1002/2014JB011457.

Gao, H., D. A. Schmidt, and R. J. Weldon (2012), Scaling relationships of source parameters for slow slip events, *Bull. Seismol. Soc. Am.*, *102*(1), 352–360, doi:10.1785/0120110096.

Ghosh, A., J. E. Vidale, J. R. Sweet, K. C. Creager, A. G. Wech, H. Houston, and E. E. Brodsky (2010a), Rapid, continuous streaking of tremor in Cascadia, *Geochem. Geophys. Geosyst.*, *11*, Q12010, doi:10.1029/2010GC003305.

Ghosh, A., J. E. Vidale, J. R. Sweet, K. C. Creager, A. G. Wech, and H. Houston (2010b), Tremor bands sweep Cascadia, *Geophys. Res. Lett.*, *37*, L08301, doi:10.1029/2009GL042301.

Ghosh, A., E. Huesca-Pérez, E. Brodsky, and Y. Ito (2015), Very low frequency earthquakes in Cascadia migrate with tremor, *Geophys. Res. Lett.*, *42*, 3228–3232, doi:10.1002/2015GL063286.

Gladwin, M. T., R. L. Gwyther, R. H. G. Hart, and K. S. Breckenbridge (1994), Measurements of the strain field associated with episodic creep events on the San Andreas fault at San Juan Bautista, California, *J. Geophys. Res.*, *99*, 4559–4565, doi:10.1029/93JB02877.

Hansen, R. T., M. G. Bostock, and N. I. Christensen (2012), Nature of the low velocity zone in Cascadia from receiver function waveform inversion, *Earth Planet. Sci. Lett.*, *337–338*, 25–38, doi:10.1016/j.epsl.2012.05.031.

Hawthorne, J. C., and A. M. Rubin (2010), Tidal modulation of slow slip in Cascadia, *J. Geophys. Res.*, *115*, B09406, doi:10.1029/2010JB007502.

Hawthorne, J. C., and A. M. Rubin (2013a), Tidal modulation and back-propagating fronts in slow slip events simulated with a velocity-weakening to velocity-strengthening friction law, *J. Geophys. Res.*, *118*, 1216–1239, doi:10.1002/jgrb.50107.

Hawthorne, J. C., and A. M. Rubin (2013b), Short-time scale correlation between slow slip and tremor in Cascadia, *J. Geophys. Res.*, *118*, 1316–1329, doi:10.1002/jgrb.50103.

Hawthorne, J. C., and A. M. Rubin (2013c), Laterally propagating slow slip events in a rate and state friction model with a velocity-weakening to velocity-strengthening transition, *J. Geophys. Res.*, *118*, 3785–3808, doi:10.1002/jgrb.50261.

Hodgkinson, K., J. Langbein, B. Henderson, D. Mencin, and A. Borsa (2013), Tidal calibration of plate boundary observatory borehole strainmeters, *J. Geophys. Res. Solid Earth*, *118*, 447–458, doi:10.1029/2012JB009651.

Houston, H. (2015), Low friction and fault weakening revealed by rising sensitivity of tremor to tidal stress, *Nat. Geosci.*, *8*(5), 409–415, doi:10.1038/ngeo2419.

Houston, H., B. G. Delbridge, A. G. Wech, and K. C. Creager (2011), Rapid tremor reversals in Cascadia generated by a weakened plate interface, *Nat. Geosci.*, *4*(6), 404–409, doi:10.1038/ngeo1157.

Hutchison, A. A., and A. Ghosh (2016), Very low frequency earthquakes spatiotemporally asynchronous with strong tremor during the 2014 episodic tremor and slip event in Cascadia, *Geophys. Res. Lett.*, *43*, 6876–6882, doi:10.1002/2016GL069750.

Ide, S. (2010), Striations, duration, migration and tidal response in deep tremor, *Nature*, *466*(7304), 356–359, doi:10.1038/nature09251.

Kao, H., S. J. Shan, H. Dragert, G. Rogers, J. F. Cassidy, and K. Ramachandran (2005), A wide depth distribution of seismic tremors along the northern Cascadia margin, *Nature*, *436*(7052), 841–844, doi:10.1038/nature03903.

Kao, H., S.-J. Shan, H. Dragert, G. Rogers, J. F. Cassidy, K. Wang, T. S. James, and K. Ramachandran (2006), Spatial-temporal patterns of seismic tremors in northern Cascadia, *J. Geophys. Res.*, *111*, B03309, doi:10.1029/2005JB003727.
Kao, H., S.-J. Shan, H. Dragert, and G. Rogers (2009), Northern Cascadia episodic tremor and slip: A decade of tremor observations from 1997 to 2007, *J. Geophys. Res.*, *114*, B00A12, doi:10.1029/2008JB006046.
Krogstad, R., and D. A. Schmidt (2015), Assessing the updip spatial offset of tremor and slip during ETS events in Cascadia, Abstract S31A–2721 presented at 2015 Fall Meeting, AGU, San Francisco, Calif.
Langbein, J. (2004), Noise in two-color electronic distance meter measurements revisited, *J. Geophys. Res.*, *109*, B04406, doi:10.1029/2003JB002819.
Langbein, J. (2010), Computer algorithm for analyzing and processing borehole strainmeter data, *Comput. Geosci.*, *36*(5), 611–619, doi:10.1016/j.cageo.2009.08.011, 00008.
Langbein, J. (2015), Borehole strainmeter measurements spanning the 2014 Mw6.0 South Napa Earthquake, California: The effect from instrument calibration, *J. Geophys. Res.*, *120*, 7190–7202, doi:10.1002/2015JB012278.
Lawn, B. (1993), *Fracture of Brittle Solids*, 2nd ed., Cambridge Univ. Press, Cambridge, U. K.
Linde, A. T., K. Suyehiro, S. Miura, I. S. Sacks, and A. Takagi (1988), Episodic aseismic earthquake precursors, *Nature*, *334*(6182), 513–515, doi:10.1038/334513a0.
Linde, A. T., M. T. Gladwin, M. J. S. Johnston, R. L. Gwyther, and R. G. Bilham (1996), A slow earthquake sequence on the San Andreas fault, *Nature*, *383*, 65–68, doi:10.1038/383065a0.
Liu, Y., and A. M. Rubin (2010), Role of fault gouge dilatancy on aseismic deformation transients, *J. Geophys. Res.*, *115*, B10414, doi:10.1029/2010JB007522.
Luo, Y., and J. P. Ampuero (2011), Numerical simulation of tremor migration triggered by slow slip and rapid tremor reversals, in Abstract S33C–02 presented at 2011 Fall Meeting, AGU, San Francisco, Calif.
McCrory, P. A., J. L. Blair, F. Waldhauser, and D. H. Oppenheimer (2012), Juan de Fuca slab geometry and its relation to Wadati-Benioff zone seismicity, *J. Geophys. Res.*, *117*, B09306, doi:10.1029/2012JB009407.
Nowack, R. L., and M. G. Bostock (2013), Scattered waves from low-frequency earthquakes and plate boundary structure in northern Cascadia, *Geophys. Res. Lett.*, *40*, 4238–4243, doi:10.1002/grl.50826.
Obara, K. (2010), Phenomenology of deep slow earthquake family in southwest Japan: Spatiotemporal characteristics and segmentation, *J. Geophys. Res.*, *115*, B00A25, doi:10.1029/2008JB006048.
Okada, Y. (1985), Surface deformation due to shear and tensile faults in a half-space, *Bull. Seismol. Soc. Am.*, *75*(4), 1135–1154.
Peng, Y., and A. M. Rubin (2016), High-resolution images of tremor migrations beneath the Olympic Peninsula from stacked array of arrays seismic data, *Geochem. Geophys. Geosyst.*, *17*, 587–601, doi:10.1002/2015GC006141.
Peng, Y., A. M. Rubin, M. G. Bostock, and J. G. Armbruster (2015), High-resolution imaging of rapid tremor migrations beneath southern Vancouver Island using cross-station cross correlations, *J. Geophys. Res.*, *120*, 4317–4332, doi:10.1002/2015JB011892.
Peng, Z., D. R. Shelly, and W. L. Ellsworth (2015), Delayed dynamic triggering of deep tremor along the Parkfield-Cholame section of the San Andreas Fault following the 2014 M6.0 South Napa earthquake, *Geophys. Res. Lett.*, *42*, 7916–7922, doi:10.1002/2015GL065277.
Radiguet, M., F. Cotton, M. Vergnolle, M. Campillo, A. Walpersdorf, N. Cotte, and V. Kostoglodov (2012), Slow slip events and strain accumulation in the Guerrero gap, Mexico, *J. Geophys. Res.*, *117*, B04305, doi:10.1029/2011JB008801.
Roeloffs, E. (2010), Tidal calibration of plate boundary observatory borehole strainmeters: Roles of vertical and shear coupling, *J. Geophys. Res.*, *115*, B06405, doi:10.1029/2009JB006407.
Roeloffs, E. (2015), Constraining aseismic slip in the Cascadia subduction zone with Plate Boundary Observatory borehole strainmeters in northern Oregon, Abstract S31A–2723 presented at 2015 Fall Meeting, AGU, San Francisco, Calif.
Royer, A. A., and M. G. Bostock (2014), A comparative study of low frequency earthquake templates in northern Cascadia, *Earth Planet. Sci. Lett.*, *402*, 247–256, doi:10.1016/j.epsl.2013.08.040.
Royer, A. A., A. M. Thomas, and M. G. Bostock (2015), Tidal modulation and triggering of low-frequency earthquakes in northern Cascadia, *J. Geophys. Res.*, *120*, 384–405, doi:10.1002/2014JB011430.
Rubin, A. M. (2011), Designer friction laws for bimodal slow slip propagation speeds, *Geochem. Geophys. Geosyst.*, *12*, Q04007, doi:10.1029/2010GC003386.
Rubin, A. M., and J. P. Ampuero (2005), Earthquake nucleation on (aging) rate and state faults, *J. Geophys. Res.*, *110*, B11312, doi:10.1029/2005JB003686.
Rubin, A. M., and J.-P. Ampuero (2009), Self-similar slip pulses during rate-and-state earthquake nucleation, *J. Geophys. Res.*, *114*, B11305, doi:10.1029/2009JB006529.
Rubin, A. M., and J. G. Armbruster (2013), Imaging slow slip fronts in Cascadia with high precision cross-station tremor locations, *Geochem. Geophys. Geosyst.*, *14*, 5371–5392, doi:10.1002/2013GC005031.
Ryberg, T., C. Haberland, G. S. Fuis, W. L. Ellsworth, and D. R. Shelly (2010), Locating non-volcanic tremor along the San Andreas Fault using a multiple array source imaging technique, *Geophys. J.*, *183*(3), 1485–1500, doi:10.1111/j.1365-246X.2010.04805.x.
Savard, G., and M. G. Bostock (2015), Detection and location of low-frequency earthquakes using cross-station correlation, *Bull. Seismol. Soc. Am.*, *105*(4), 2128–2142, doi:10.1785/0120140301.
Schmidt, D. A., and H. Gao (2010), Source parameters and time-dependent slip distributions of slow slip events on the Cascadia subduction zone from 1998 to 2008, *J. Geophys. Res.*, *115*, B00A18, doi:10.1029/2008JB006045.
Segall, P., A. M. Rubin, A. M. Bradley, and J. R. Rice (2010), Dilatant strengthening as a mechanism for slow slip events, *J. Geophys. Res.*, *115*, B12305, doi:10.1029/2010JB007449.
Shelly, D. R. (2009), Possible deep fault slip preceding the 2004 Parkfield earthquake, inferred from detailed observations of tectonic tremor, *Geophys. Res. Lett.*, *36*, L17318, doi:10.1029/2009GL039589.
Shelly, D. R. (2010), Migrating tremors illuminate complex deformation beneath the seismogenic San Andreas fault, *Nature*, *463*(7281), 648–652, doi:10.1038/nature08755.
Shibazaki, B., and T. Shimamoto (2007), Modelling of short-interval silent slip events in deeper subduction interfaces considering the frictional properties at the unstable-stable transition regime, *Geophys. J.*, *171*(1), 191–205, doi:10.1111/j.1365-246X.2007.03434.x.
Sun, W.-F., Z. Peng, C.-H. Lin, and K. Chao (2015), Detecting deep tectonic tremor in Taiwan with a dense array, *Bull. Seismol. Soc. Am.*, *105*(3), 1349–1358, doi:10.1785/0120140258.
Szeliga, W., T. Melbourne, M. Santillan, and M. Miller (2008), GPS constraints on 34 slow slip events within the Cascadia subduction zone, 1997-2005, *J. Geophys. Res.*, *113*, B04404, doi:10.1029/2007JB004948.
Tamura, Y., T. Sato, M. Ooe, and M. Ishiguro (1991), A procedure for tidal analysis with a Bayesian information criterion, *Geophys. J.*, *104*(3), 507–516, doi:10.1111/j.1365-246X.1991.tb05697.x.

Thomas, T. W., J. E. Vidale, H. Houston, K. C. Creager, J. R. Sweet, and A. Ghosh (2013), Evidence for tidal triggering of high-amplitude rapid tremor reversals and tremor streaks in northern Cascadia, *Geophys. Res. Lett.*, *40*, 4254–4259, doi:10.1002/grl.50832.

Ueno, T., T. Maeda, K. Obara, Y. Asano, and T. Takeda (2010), Migration of low-frequency tremors revealed from multiple-array analyses in western Shikoku, Japan, *J. Geophys. Res.*, *115*, B00A26, doi:10.1029/2008JB006051.

Wang, K., H. Dragert, H. Kao, and E. Roeloffs (2008), Characterizing an "uncharacteristic" ETS event in northern Cascadia, *Geophys. Res. Lett.*, *35*, L15303, doi:10.1029/2008GL034415.

Wech, A. G., and N. M. Bartlow (2014), Slip rate and tremor genesis in Cascadia, *Geophys. Res. Lett.*, *41*, 392–398, doi:10.1002/2013GL058607.

Wech, A. G., and K. C. Creager (2007), Cascadia tremor polarization evidence for plate interface slip, *Geophys. Res. Lett.*, *34*, L22306, doi:10.1029/2007GL031167.

Wech, A. G., and K. C. Creager (2008), Automated detection and location of Cascadia tremor, *Geophys. Res. Lett.*, *35*, L20302, doi:10.1029/2008GL035458.

Wech, A. G., K. C. Creager, and T. I. Melbourne (2009), Seismic and geodetic constraints on Cascadia slow slip, *J. Geophys. Res.*, *114*, B10316, doi:10.1029/2008JB006090.